Improving the magnetic properties of Nd–Fe–B sintered magnets by the grain boundary diffusion of Pr-LRE-Tb-Cu-Al (LRE = None, La, Nd, and Ce) alloys using stamp coating

Dong Hyun Lee [a,b], Seong Chan Kim [a], Hyeonjong Jeong [a], Vitalii Galkin [a,b], Jung Woo Ha [a], Juyoung Baek [a], Tae-Young Yun [a], Jong Tae Kim [a], Seok-Hwan Chung [a], Sumin Kim [c], Donghwan Kim [d], Sang Hyub Lee [d], Jong Wook Roh [b,*], Dong Hwan Kim [a,**], Jeongmin Kim [a,***]

[a] *Division of Nanotechnology, DGIST, 333 Techno Jungang-daero, Hyeonpung-eup, Dalseong-gun, Daegu, 42988, Republic of Korea*
[b] *Department of Hydrogen and Renewable Energy, Kyungpook National University, Daegu, 41566, Republic of Korea*
[c] *Department of Magnetic Materials, Korea Institute of Materials Science, Changwon, 51508, Republic of Korea*
[d] *R&D Center, Star Group, Daegu, 42714, Republic of Korea*

ARTICLE INFO

ABSTRACT

Nd–Fe–B sintered magnets exhibit a high maximum energy product and have been utilized in a wide range of applications. Herein, we report that the stamp coating method using powder-type diffusion sources improves the magnetic properties of Nd–Fe–B sintered magnets through the grain boundary diffusion (GBD) process. Compared with the conventional dip-coating method based on slurry-type diffusion sources, stamp coating provided a comparable coercivity improvement with simplified processing. Based on the stamp coating method, diffusion sources in which 80 wt% of heavy rare-earth (HRE) elements were substituted with light rare-earth (LRE) elements and transition metals were investigated. The $Pr_{60}Tb_{20}Cu_{15}Al_5$-GBD magnet exhibited magnetic properties comparable to those of a pure Tb-GBD magnet, while significantly reducing Tb usage. Moreover, in pursuit of a more cost-effective diffusion source, $Pr_{40}LRE_{20}Tb_{20}Cu_{15}Al_5$-GBD magnets (LRE = La, Nd, Ce) with the additional partial substitution of expensive Pr were evaluated. The increase in coercivity per Tb usage (kOe/wt.% Tb) of the $Pr_{60}Tb_{20}Cu_{15}Al_5$- and $Pr_{40}LRE_{20}Tb_{20}Cu_{15}Al_5$-GBD magnets (~20 kOe/wt.%) were considerably higher than those of Tb_{100}-GBD magnets (6.4 kOe/wt.%). Furthermore, the Tb-reduced GBD magnets showed improved thermal stability compared to that of the Tb-GBD magnet. These findings demonstrate that the cost of the GBD process can be effectively reduced through stamp coating and the substitution of costly HRE and LRE elements, thereby providing a promising strategy for the development of high-performance Nd–Fe–B sintered magnets.

1. Introduction

Since their discovery in the 1980s, Nd–Fe–B sintered magnets with a high maximum energy product ($(BH)_{max}$) have been utilized in a wide range of applications, including hard disk drives, traction motors, and wind power generators [1,2]. However, extensive efforts are underway to improve their magnetic properties and thermal stability [3–7]. In particular, Nd–Fe–B sintered magnets for eco-friendly automobile

motors require high coercivity (H_{cj}) at room temperature to maintain stable performance at high operating temperatures exceeding 150 °C [8]. By substituting Nd in the $Nd_2Fe_{14}B$ main phase with heavy rare-earth (HRE) elements such as Tb and Dy, their H_{cj} and thermal stability are effectively enhanced owing to the high anisotropy field (H_a) of $HRE_2Fe_{14}B$ phases [9]. However, HRE substitution reduces the remanence (B_r) owing to antiferromagnetic coupling between the HRE and Fe atoms [10]. Moreover, as the cost of applying HREs increases and
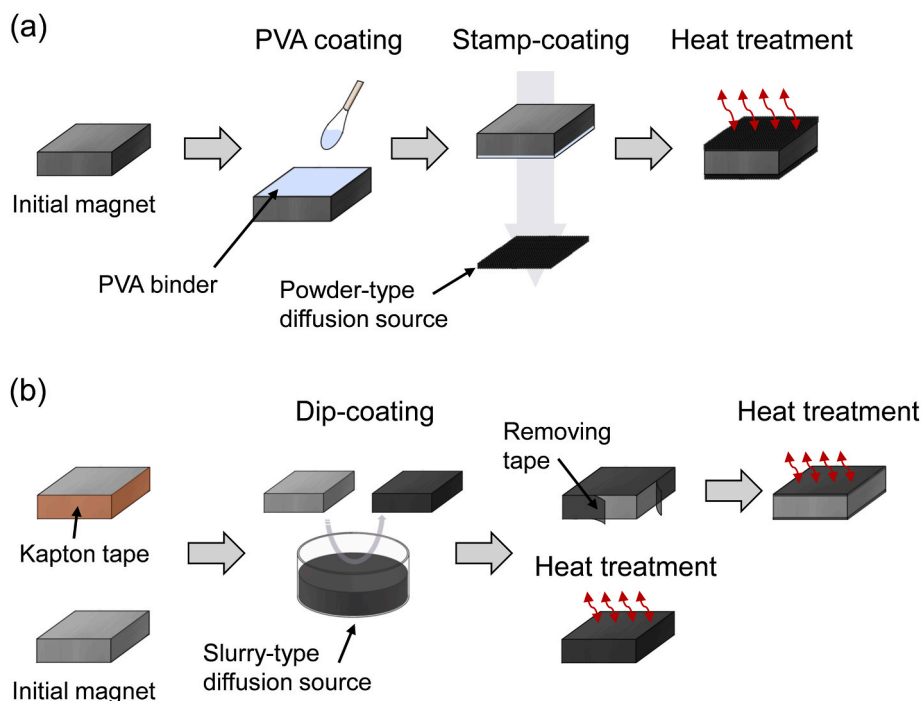
Fig. 1. Schematic of the (a) stamp and (b) dip coating processes of diffusion sources for GBD Nd–Fe–B sintered magnets.

their availability decreases, the development of processes that can minimize the use of HREs in high-performance Nd–Fe–B sintered magnets is inevitable [3].

Accordingly, a grain boundary diffusion (GBD) process was developed, in which HREs are applied to magnet surfaces and then heat-treated to allow them to infiltrate the magnet interior [7]. This process forms a $HRE_2Fe_{14}B$ shell on the surface of the $Nd_2Fe_{14}B$ grains while maintaining the composition of the grain core, effectively increasing H_{cj} while preventing a significant decrease in the remanence of the magnet [4,11]. Furthermore, compared to conventional alloying methods, GBD has led to a dramatic reduction in HRE usage for high-performance Nd–Fe–B sintered magnets by applying it only to magnetically vulnerable areas [4]. However, GBD requires coating the magnet surface with a diffusion source, which inevitably leads to HRE waste. Various coating methods have been employed to distribute the diffusion source evenly on the magnet surface, including powder coating [12], dip coating [13], evaporation [11], melt-spun ribbons [14], magnetron sputtering [15], spray coating [16], and electrophoretic deposition [17].

Wet methods based on a slurry-type diffusion source, such as dip and spray coatings, are suitable for mass production; however, it is difficult to precisely control the coating surface, leading to the unnecessary consumption of diffusion sources [13,16]. Moreover, the considerable slurry waste generated during the diffusion process requires consideration of recovery procedures. In contrast, the powder-based dry method enables the precise application of the required amount of coating on the desired surface of the magnet, thereby reducing the waste of diffusion sources [18]. Moreover, this approach eliminates the need for solution-based slurry processes and allows for the convenient application of atmospheric control, including vacuum control, which mitigates the risk of oxidation of the diffusion sources. In addition, applying a binder prior to the powder coating can improve the uniformity of the coating layer and enhance the adhesion between the diffusion source and magnet surface [19,20].

Another approach for reducing the use of HREs in GBD is to substitute them in the diffusion source with more economical light rare-earth (LRE) elements, such as La, Ce, Pr, and Nd—a strategy that has been widely investigated [6,14,21,22]. In particular, Pr, which exhibits the highest H_a among LREs, has been reported to effectively enhance the

coercivity of Nd–Fe–B sintered magnets during GBD by modifying the grain boundary microstructure and forming a Pr-containing shell on the grain surface [23,24]. However, despite the effectiveness of Pr in substituting HREs, its relatively higher cost compared with other LREs constrains its contribution to reducing the overall production cost of Nd–Fe–B sintered magnets [25].

In this study, we propose a stamp coating technique based on a powder-type diffusion source suitable for mass production in the GBD process, develop a Pr-substituted diffusion source to reduce the consumption of HREs, and further investigate the appropriate LRE element to minimize the use of Pr. The feasibility of the stamp coating method was demonstrated through a systematic comparison of the magnetic property improvements of stamp- and dip-coated GBD magnets. A Tb-reduced diffusion source was prepared using 60 wt% Pr and 20 wt% transition metals ($Pr_{60}Tb_{20}Cu_{15}Al_5$), and the improvement in the magnetic properties of stamp-coated $Pr_{60}Tb_{20}Cu_{15}Al_5$-GBD magnets was quantitatively evaluated. The optimal GBD parameters were established through a systematic analysis of the dependence of the magnetic properties on the GBD temperature and time, followed by a detailed investigation of the microstructural characteristics, including elemental distribution profiles. To explore the possibility of further reducing the Pr consumption, three diffusion sources containing 20 wt% LRE were examined ($Pr_{40}LRE_{20}Tb_{20}Cu_{15}Al_5$, LRE = La, Nd, and Ce). The $Pr_{60}Tb_{20}Cu_{15}Al_5$-GBD magnet exhibited magnetic properties comparable to those of pure Tb-GBD magnets, despite the 80 wt% reduction in Tb usage, and La was identified as the most suitable substitute for Pr, highlighting the potential of this approach for the cost-effective development of high-performance Nd–Fe–B sintered magnets.

2. Experimental

Commercial N52 grade HRE-free Nd–Fe–B sintered magnets ($12 \times 12 \times 5$ mm^3) with a composition $Nd_{21.29}Pr_{6.03}Fe_{70.69}B_{0.94}Co_{0.44}M_{bal}$ (M = Cu, Al, Zn, Ga) (wt.%) were used as the initial magnets. To obtain the diffusion sources for the GBD process, Tb, $Pr_{60}Tb_{20}Cu_{15}Al_5$, and $Pr_{40}LRE_{20}Tb_{20}Cu_{15}Al_5$ (LRE = La, Nd, and Ce) ingots were prepared by induction melting, followed by melt spinning. The melt-spun metal and alloy ribbons were subsequently pulverized into fine powders via
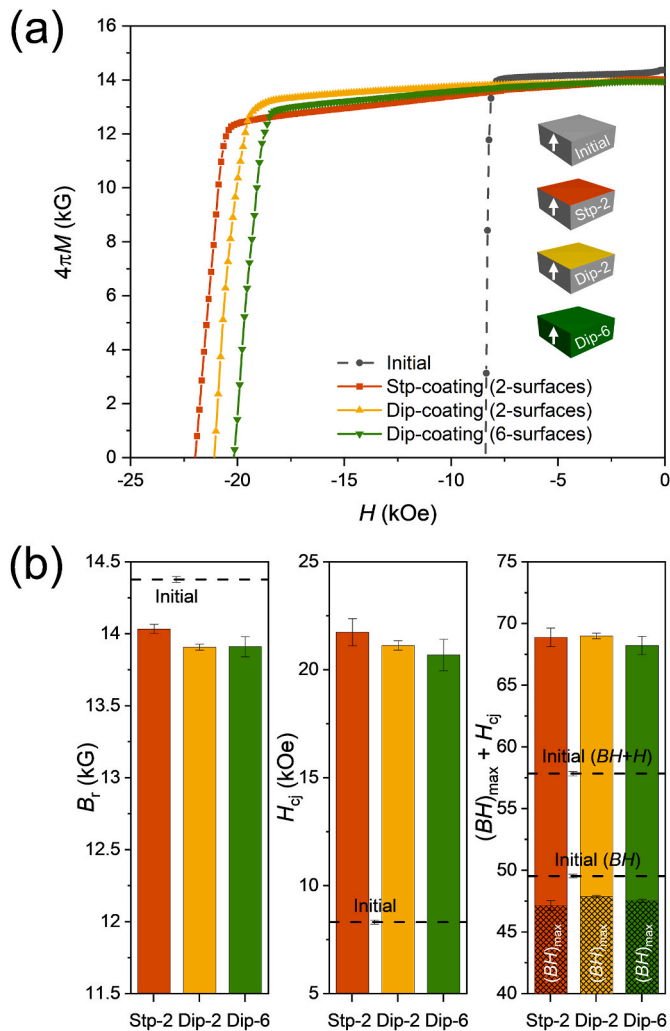
Fig. 2. Magnetic properties of GBD magnets depending on the coating method. (a) Representative demagnetization curves of stamp- (stp) 2-surfaces dip-, 6-surfaces dip-coated, and initial magnets. The white arrows in the magnet schematics indicate the magnetic alignment (*c* axis). (b) Average values of B_r, H_{cj}, and $(BH)_{max} + H_{cj}$ obtained from multiple samples of stamp-, 2-surfaces dip-, and 6-surfaces dip-coated, and initial magnets. The patterned bars represent $(BH)_{max}$.

hydrogenation and hand milling under H_2 and Ar atmospheres, respectively. The hydrogenated powders were sieved (53 μm) under an Ar atmosphere. For the stamp coating of the diffusion sources, the top and bottom surfaces (normal to the magnetic alignment) of the initial magnets were first coated with a polyvinyl alcohol (PVA) binder solution via brush coating. Subsequently, the magnet was vertically stamped onto the uniformly spread powder-type sources, corresponding to 0.5 wt % of the magnet weight for each surface (1 wt% in total), under an applied pressure of approximately 15 kPa (Fig. 1(a)). For dip-coating, slurry-type diffusion sources were prepared by mixing the powder with anhydrous ethanol at a mass ratio of 1:4. For the selective coating of the surface, the sides of the magnets were masked with Kapton tape (Fig. 1(b)). A constant loading of 1 wt% diffusion source was applied to all the dip-coated magnets. For the GBD of sources, the coated magnets were subjected to heat treatment in the temperature range of 750–900 °C for 6 h, followed by annealing at 450 °C for 3 h under vacuum (10^{-6} Torr). Blank magnets (without a diffusion source) were prepared by heat treatment at 850 °C for 6 h and annealing.

The magnetic properties of the initial and GBD magnets were measured at room temperature using a *BH* hysteresis-loop tracer

(Permagraph C-300; Magnet-Physik). More than four samples were used to obtain the average value of the magnetic properties and the standard deviation for each GBD process and diffusion source. Thermal stability was evaluated in the temperatures range of 25–200 °C using the high-temperature poles of the *BH* tracer. The phase compositions and crystal structures of the GBD magnets were confirmed using X-ray diffraction (XRD; EMPYREAN, PANalytical). Microstructural analysis, including elemental distribution analysis, was performed using scanning electron microscopy (SEM; SU8220, Hitachi) and field-emission electron probe microanalysis (EPMA, JAX8530F, JEOL).

3. Results and discussion

First, to test the feasibility of stamp coating the diffusion source in the GBD process, the dependence of the magnetic properties on the coating method was investigated using 1 wt% Tb. Fig. 2(a) shows the demagnetization curves of the initial magnet and Tb-diffused magnets prepared with different coating methods. For stamp coating, a PVA binder was introduced to enhance the density and uniformity of the diffusion source distribution coated on the magnet surfaces [19,20]. Subsequently, the powder-type source was stamped on the top and bottom surfaces (Fig. 1(a)). The coated surfaces are perpendicular to the magnetic alignment of the magnet (*c* axis), which is the preferred plane for improving the GBD efficiency [16,26]. For systematic comparison, typical dip-coated samples were prepared with a slurry-type source (6-surfaces dip-coating), and partial surface dip-coating was conducted using the masking technique (2-surfaces dip-coating), as shown in Fig. 1 (b). For all the types of coatings, the increase in weight after drying was 1 wt% of the initial magnet.

Fig. 2(b) shows the variation in the magnetic properties after GBD of the initial and stamp-, 2-surfaces dip-, and 6-surfaces dip-coated magnets. The remanence of the stamp-coated magnet was slightly higher than those of the dip-coated magnets (<1 %), but a noticeable dependency on the number of coated surfaces was not obtained between the different dip-coated samples (<0.03 %). This suggests that the variations in the coating method and coated surface did not significantly affect the remanence. Conversely, the differences in coercivity according to the coating method and number of coated surfaces were not negligible. The average coercivity of the 2-surfaces dip-coated magnet was approximately 2 % higher than that of the 6-surfaces dip-coated magnet. Moreover, the average coercivity of the stamp-coated magnet was approximately 3 % higher than that of the 2-surfaces dip-coated magnet with the coating on the same surfaces.

As mentioned above, in GBD using the same amount of diffusion source, an additional increase in coercivity can be expected by coating the surfaces normal to the magnetic alignment [16]. This is because the travel distance and energy barrier for HRE diffusion within the Nd–Fe–B matrix are smaller in the direction perpendicular to the *c* axis than in the parallel direction [26]. Therefore, the diffusion efficiency can be increased by minimizing the consumption of the source caused by lattice diffusion based on selective coating of the top and bottom surfaces. As a result, higher coercivity and improved squareness were achieved in the selectively coated magnets (2-surfaces dip-coated) compared with those coated on all surfaces (6-surfaces dip-coated). The additional increase observed for the stamp-coated magnets can be attributed to the PVA binder, which increases the binding force and enhances the coating efficiency by forming a dense and uniform coating layer [19].

The superiority of stamp coating in the GBD process was determined using the combined $(BH)_{max}$ and H_{cj} values, which is a comprehensive index for evaluating the performance of permanent magnets ($(BH)_{max} + H_{cj}$) [27]. As shown in Fig. 2(a), the stamp-coated magnet exhibited a slight decrease in the squareness of the hysteresis loop compared with the dip-coated magnets. This is accompanied by an increase in coercivity and is explained by differences in reversal magnetic fields depending on the depth from the surface [28]. As a result, the $(BH)_{max}$ of the stamp-coated magnet was 1.5 % and 1 % lower than those of the
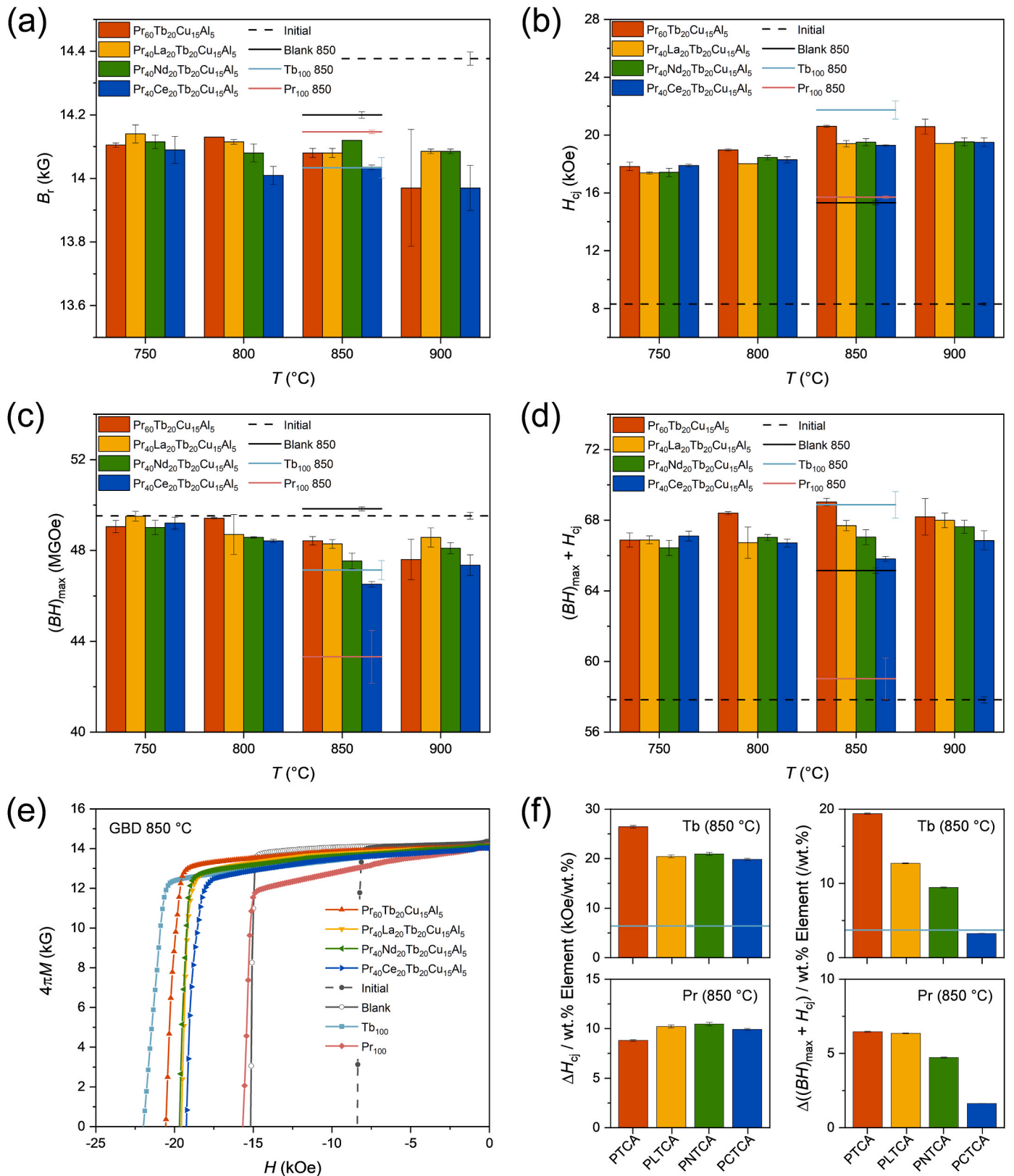
Fig. 3. Magnetic properties of Nd–Fe–B sintered magnets depending on GBD temperatures and diffusion sources. Average values of (a) B_r, (b) H_{cj}, (c) $(BH)_{max}$, and (d) $(BH)_{max} + H_{cj}$ of $Pr_{60}Tb_{20}Cu_{15}Al_5$-, $Pr_{40}La_{20}Tb_{20}Cu_{15}Al_5$-, $Pr_{40}Nd_{20}Tb_{20}Cu_{15}Al_5$-, and $Pr_{40}Ce_{20}Tb_{20}Cu_{15}Al_5$-GBD magnets heat treated at different temperatures. The magnetic properties of the initial and blank, Tb_{100}-, and Pr_{100}-GBD magnets following 850 °C heat treatment are also shown. (e) Representative demagnetization curves of the initial, blank, and GBD magnets. (f) Changes in H_{cj} and $(BH)_{max} + H_{cj}$ per Tb and Pr usage of 850 °C heat-treated GBD magnets. PTCA, PLTCA, PNTCA, and PCTCA indicate $Pr_{60}Tb_{20}Cu_{15}Al_5$, $Pr_{40}La_{20}Tb_{20}Cu_{15}Al_5$, $Pr_{40}Nd_{20}Tb_{20}Cu_{15}Al_5$, and $Pr_{40}Ce_{20}Tb_{20}Cu_{15}Al_5$, respectively. The properties of the Tb_{100}-GBD magnet are indicated by light blue lines.

Table 1

Magnetic properties obtained from multiple samples of initial, blank, and GBD magnets.

| Magnets (GBD @ 850 °C)	B_r (kG)	H_{cj} (kOe)	$(BH)_{max}$ (MGOe)	$(BH)_{max} + H_{cj}$ (MGOe + kOe)	ΔH_{cj}/Tb (kOe/wt.%)	ΔH_{cj}/Pr (kOe/wt.%)
Initial	14.37 ± 0.02	8.31 ± 0.09	49.52 ± 0.15	57.83 ± 0.17	–	–
Blank	14.20 ± 0.01	15.32 ± 0.14	49.83 ± 0.09	65.15 ± 0.16	–	–
Tb_{100}	14.03 ± 0.03	21.74 ± 0.62	47.14 ± 0.41	68.88 ± 0.75	6.42 ± 0.19	–
Pr_{100}	14.14 ± 0.01	15.71 ± 0.11	43.32 ± 1.17	59.02 ± 1.17	–	–
$Pr_{60}Tb_{20}Cu_{15}Al_5$	14.08 ± 0.01	20.6 ± 0.06	45.43 ± 0.19	69.03 ± 0.2	26.41 ± 0.25	8.81 ± 0.08
$Pr_{40}La_{20}Tb_{20}Cu_{15}Al_5$	14.08 ± 0.01	19.41 ± 0.21	48.29 ± 0.19	67.69 ± 0.29	20.44 ± 0.29	10.22 ± 0.14
$Pr_{40}Nd_{20}Tb_{20}Cu_{15}Al_5$	14.12 ± 0.00	19.51 ± 0.25	47.54 ± 0.35	67.04 ± 0.43	20.94 ± 0.32	10.47 ± 0.16
$Pr_{40}Ce_{20}Tb_{20}Cu_{15}Al_5$	13.97 ± 0.07	19.29 ± 0.06	46.52 ± 0.12	65.81 ± 0.13	19.86 ± 0.18	9.93 ± 0.09

2-surfaces and 6-surfaces dip-coated magnets, respectively. Therefore, the average $(BH)_{max} + H_{cj}$ value of the stamp-coated magnet was comparable to that of the 2-surfaces dip-coated magnet and 1 % higher than that of the conventional dip-coated magnets (6-surfaces).

To reduce the HRE usage and increase the GBD efficiency, stamp coating-based GBD was performed using powder-type diffusion sources containing LREs and transition metals. Pr was used to replace Tb, and Cu and Al were added to promote the GBD efficiency, based on our previous results [29]. We also tested alternative LREs to partially replace Pr, namely, La, Nd, and Ce. Fig. 3(a–d) show the dependence of the magnetic properties on the GBD temperature from 750 to 900 °C for 6 h using 1 wt% $Pr_{60}Tb_{20}Cu_{15}Al_5$, $Pr_{40}La_{20}Tb_{20}Cu_{15}Al_5$, $Pr_{40}Nd_{20}Tb_{20}Cu_{15}Al_5$, and $Pr_{40}Ce_{20}Tb_{20}Cu_{15}Al_5$. In all the GBD magnets, a decrease in B_r compared to that of the initial magnet and a weak temperature dependence that differed depending on the diffusion source were observed (Fig. 3(a)). In the case of H_{cj}, a distinct increase was observed compared to that of the initial magnet, with an increasing trend as the GBD temperature increased, but saturated above 850 °C (Fig. 3(b)). In contrast, the $(BH)_{max}$ of the GBD magnets were slightly lower compared with that of the initial magnet, and a decreasing trend was observed as the GBD temperature increased (Fig. 3(c)). The combined $(BH)_{max} + H_{cj}$ values were used to evaluate the optimal GBD temperature and diffusion source (Fig. 3(d)). The $Pr_{60}Tb_{20}Cu_{15}Al_5$-GBD magnet with Tb replaced by Pr and transition metals showed the highest $(BH)_{max} + H_{cj}$ value at a GBD temperature of 850 °C, and La was found to be the most effective alternative LRE element for Pr.

Fig. 3(e) shows representative demagnetization curves of the initial, blank and $Pr_{60}Tb_{20}Cu_{15}Al_5$-, $Pr_{40}La_{20}Tb_{20}Cu_{15}Al_5$-, $Pr_{40}Nd_{20}Tb_{20}Cu_{15}Al_5$-, $Pr_{40}Ce_{20}Tb_{20}Cu_{15}Al_5$-, Tb_{100}-, and Pr_{100}-GBD magnets prepared at a GBD temperature of 850 °C; Table 1 lists the average values. Although the enhancement in H_{cj} for the GBD magnets with 80 wt% Tb reduction was lower than that for the Tb_{100}-GBD

magnet, the relatively superior squareness resulted in a higher $(BH)_{max}$, excluding the GBD magnet containing Ce (Fig. 3(c)). Moreover, a significant increase in H_{cj} was observed in the magnets with 80 wt% Tb reduction. Therefore, an additional analysis was performed to quantify the effect of lowering the usage of high-cost materials such as Tb and Pr (Fig. 3(f)). The increase in H_{cj} per Tb usage was significantly higher in all the GBD magnets ($\sim$20 kOe/wt.%) than that of the Tb_{100}-GBD magnet (6.4 kOe/wt.%), with the highest increase observed in the $Pr_{60}Tb_{20}Cu_{15}Al_5$-GBD magnet (26.4 kOe/wt.%) (Fig. 3(f), top-left panel and Table 1). The increase in $(BH)_{max} + H_{cj}$ per Tb usage was in the order of $Pr_{40}Ce_{20}Tb_{20}Cu_{15}Al_5$- (3.3/wt.%), $Pr_{40}Nd_{20}Tb_{20}Cu_{15}Al_5$- (9.5/wt.%), $Pr_{40}La_{20}Tb_{20}Cu_{15}Al_5$- (12.7/wt.%), and $Pr_{60}Tb_{20}Cu_{15}Al_5$-GBD (19.4/wt.%), and was higher than that of Tb_{100}-GBD magnet (3.7/wt.%) except for the GBD magnet containing Ce (Fig. 3(f), top-right panel). Therefore, the highest GBD efficiency was observed for the diffusion source of $Pr_{60}Tb_{20}Cu_{15}Al_5$, and La was confirmed to be the most suitable substitute for reducing the amount of Pr. The H_{cj} enhancement per Pr usage (wt.%) was higher in the $Pr_{40}La_{20}Tb_{20}Cu_{15}Al_5$-GBD magnet than in the $Pr_{60}Tb_{20}Cu_{15}Al_5$-GBD magnet (Fig. 3(f), bottom-left panel), and the enhancement of $(BH)_{max} + H_{cj}$ was confirmed to be equivalent for these two diffusion sources (Fig. 3(f), bottom-right panel).

Before elucidating the cause of the change in the magnetic properties due to the GBD process through microstructural analysis, we performed XRD analysis to confirm whether the diffusion sources of various components effectively infiltrated the magnets. Fig. 4 shows the XRD patterns of the initial and $Pr_{60}Tb_{20}Cu_{15}Al_5$-, $Pr_{40}La_{20}Tb_{20}Cu_{15}Al_5$-, $Pr_{40}Nd_{20}Tb_{20}Cu_{15}Al_5$-, $Pr_{40}Ce_{20}Tb_{20}Cu_{15}Al_5$-, and Tb_{100}-GBD magnets in the 2θ range from 20° to 80°. The peaks of the initial and GBD magnets matched well with those of the $Nd_2Fe_{14}B$ and rare earth (RE)-rich phases. The main peaks appeared in the $Nd_2Fe_{14}B$ phase, indicating that no new phase was formed during GBD (Fig. 4, left panel). The (006) diffraction peak of the Tb_{100}-GBD magnet shifts to a slightly higher angle
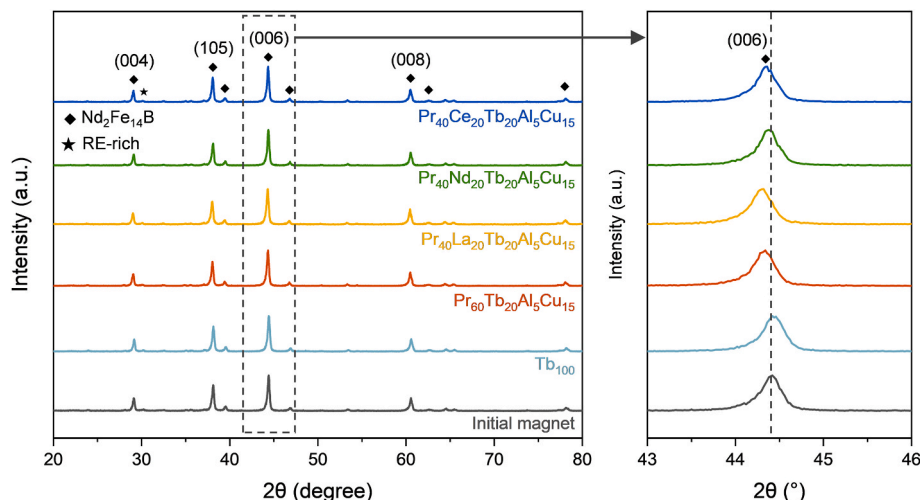
Fig. 4. XRD patterns of the initial and Tb_{100}-, $Pr_{60}Tb_{20}Cu_{15}Al_5$-, $Pr_{40}La_{20}Tb_{20}Cu_{15}Al_5$-, $Pr_{40}Nd_{20}Tb_{20}Cu_{15}Al_5$-, and $Pr_{40}Ce_{20}Tb_{20}Cu_{15}Al_5$-GBD magnets.

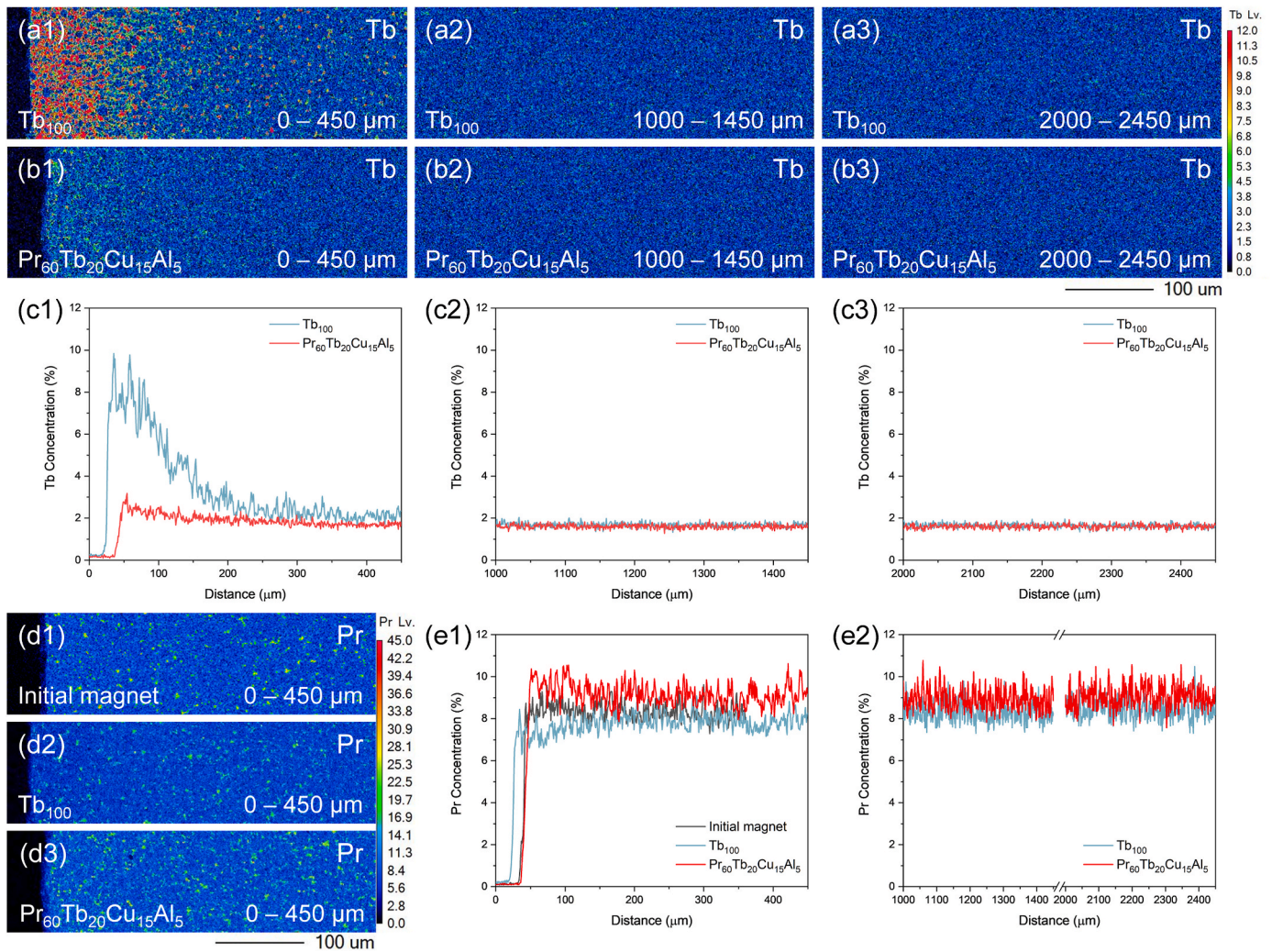**Fig. 5.** Low-magnification Tb mapping images of the (a1–a3) Tb_{100}- and (b1–b3) $Pr_{60}Tb_{20}Cu_{15}Al_5$-GBD magnets, and (c1–c3) corresponding Tb concentration profiles from the surface to the center of the magnets (0–450, 1000–1450, and 2000–2450 μm, respectively). Low-magnification Pr mapping images of the (d1) initial, (d2) Tb_{100}-GBD, and (d3) $Pr_{60}Tb_{20}Cu_{15}Al_5$-GBD magnets from the surface to a depth of 450 μm. Pr concentration profile at depths of (e1) 0–450 and (e2) 1000–1450 μm and 2000–2450 μm from the magnet surface.

than that of the initial magnet (Fig. 4, right panel). The peak angle increases as the lattice parameter decreases, according to Bragg's equation $n\lambda = 2d\sin\theta$, where n, λ, d, and θ are the diffraction order, wavelength, plane spacing, and angle between incident ray and plane, respectively [30]. Therefore, the shift of the peak positions to higher angles for the Tb_{100}-GBD sample indicates Tb diffusion into the $Nd_2Fe_{14}B$ lattice because Tb has a smaller ionic radius than Nd [31]. In contrast, when 60 wt% of the diffusion source was replaced by LREs that have larger ionic radii than Nb, the (006) diffraction peak shifted to the left compared with that of the initial magnet (Fig. 4, right panel). Moreover, the extent of the peak shift was consistent with the order of the ionic radius of the LRE (La > Ce > Pr), indicating that the diffusion source infiltrated the magnets [32].

To confirm the mechanism of the improvement in Tb utilization caused by the addition of Pr, the large-area distributions of Tb and Pr in the Tb_{100}- and $Pr_{60}Tb_{20}Cu_{15}Al_5$-GBD magnets were analyzed (Fig. 5). The low-magnification elemental mapping images and linear distribution of elements showed a distinct difference in the Tb distribution near the surface (0–450 μm), where diffusion begins (Fig. 5(al), (b1), and (c1)). Both GBD magnets exhibited the highest Tb concentration at the magnet surface; however, the concentration was more than three times higher for the Tb_{100}-GBD magnet than for the $Pr_{60}Tb_{20}Cu_{15}Al_5$-GBD magnet. This difference in Tb distribution sharply decreases with

increasing distance from the magnet surface, and a similar distribution was observed from a distance of 1000 μm (Fig. 5(a2), (b2), and (c2)) to the magnet center (Fig. 5(a3), (b3), and (c3)). Therefore, in the Tb_{100}-GBD magnet, excessive Tb consumption occurred within 200 μm from the magnet surface. In contrast, in the $Pr_{60}Tb_{20}Cu_{15}Al_5$-GBD magnet, a uniform Tb distribution was achieved without significant Tb accumulation.

The Pr distribution of the initial magnet changed before and after Tb and Pr diffusion. In the Tb_{100}-GBD magnet, a decrease in the Pr concentration was observed near the magnet surface compared to the initial magnet (Fig. 5(d1), (d2), and (e1)). These changes demonstrate that the excessive accumulation of Tb observed near the surface of the Tb_{100}-GBD magnet was caused by Tb from the diffusion source replacing Pr in the initial magnet. In contrast, $Pr_{60}Tb_{20}Cu_{15}Al_5$-GBD showed a higher Pr distribution throughout the magnet than in the initial magnet (Fig. 5 (d3), (e1), and (e2)). In particular, the Pr concentration was significantly higher than that of Tb_{100}-GBD magnet within 200 μm from the magnet surface where the Tb accumulation occurred. Therefore, it was confirmed that the addition of Pr to the diffusion source improved Tb utilization by suppressing the excessive accumulation of Tb due to Pr substitution occurring near the diffusion starting point [33].

The local microstructure was analyzed to further elucidate the mechanism of Tb accumulation observed near the magnet surface and its
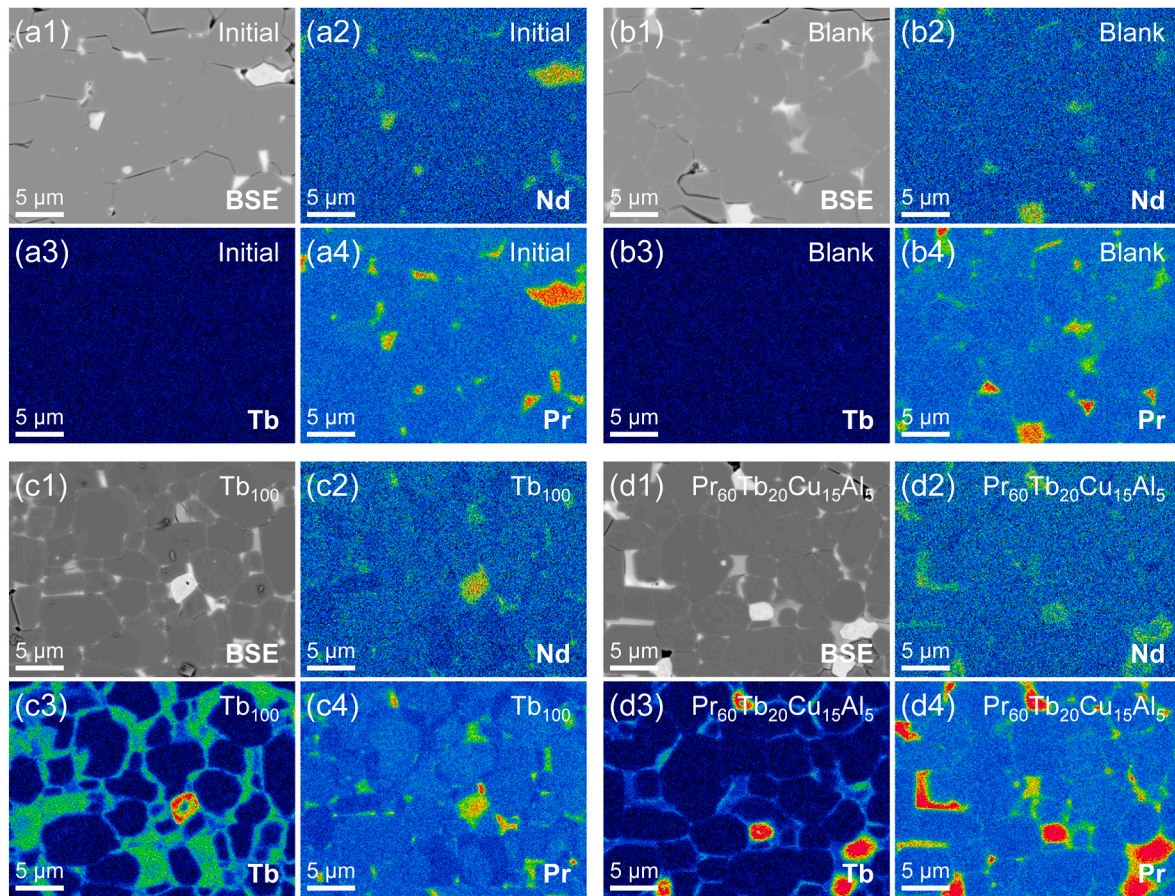
Fig. 6. High-magnification BSE-SEM and elemental mapping images of the (a) initial, (b) blank, (c) Tb$_{100}$-GBD, and (d) Pr$_{60}$Tb$_{20}$Cu$_{15}$Al$_5$-GBD magnets at 100 μm from the magnet surface. In each set of four panels, (x1) shows the BSE-SEM image, (x2) the Nd mapping, (x3) the Tb mapping, and (x4) the Pr mapping.

inhibition caused by the addition of Pr. Fig. 6 shows the local microstructure and elemental mapping at 100 μm from the magnet surface of the initial, blank, and Tb$_{100}$- and Pr$_{60}$Tb$_{20}$Cu$_{15}$Al$_5$-GBD magnets. The initial magnet exhibited no clear distinction between the Nd$_2$Fe$_{14}$B grains (dark regions) and grain boundaries, and an Nd-rich phase (bright regions) was observed at the triple junctions (Fig. 6(a1) and (a2)). Tb was absent from the initial magnet, whereas Pr was found throughout the magnet, particularly concentrated at the triple junctions (Fig. 6(a3) and (a4)). By contrast, the blank magnet, which underwent the same heat treatment as the GBD-treated magnets but without a diffusion source, exhibited continuous Nd-/Pr-rich grain boundaries between the grains of the Nd$_2$Fe$_{14}$B main phase (Fig. 6(b)). The formation of continuous nonmagnetic grain boundaries results in the magnetic decoupling of Nd$_2$Fe$_{14}$B grains, leading to enhanced coercivity, as was observed in Fig. 3(b) and (e) [34].

For the Tb$_{100}$-GBD magnet, clear core–shell structures of grains containing a Nd$_2$Fe$_{14}$B main phase (dark gray regions) and a thick Tb-rich shell (bright gray regions) were observed (Fig. 6(c1) and (c3)). This Tb-rich shell is formed by the lattice diffusion of Tb on the grain surfaces, where Tb atoms substitute Nd atoms of the Nd$_2$Fe$_{14}$B main phase (Fig. 6(c2)) [13,35]. This can be explained by the difference in the formation energy (E_f) depending on the RE of the RE$_2$Fe$_{14}$B phases; based on first-principles calculations [25], E_f = −0.034, −0.071, −0.042, −0.056, and −0.104 eV/atom for RE = La, Ce, Pr, Nd, and Tb, respectively. This variation in E_f can be attributed to lanthanide contraction, whereby E_f decreases with decreasing atomic radius, except for Ce [33]. Therefore, the lower E_f of Tb$_2$Fe$_{14}$B compared to that of Nd$_2$Fe$_{14}$B drives the spontaneous formation of a Tb-rich shell during GBD. In particular, lattice diffusion is accelerated in the initial magnet containing Pr (Fig. 6(c4)) because the E_f of Pr$_2$Fe$_{14}$B is higher than those

of Nd$_2$Fe$_{14}$B and Tb$_2$Fe$_{14}$B [25]. Therefore, as was observed in Fig. 5(a1) and (c1), excessive accumulation near the magnet surface was induced by the high Tb concentration at the diffusion starting point. This consumption of Tb in the early stage of GBD inhibited its uniform diffusion to the center of the magnet [33].

In the case of the Pr$_{60}$Tb$_{20}$Cu$_{15}$Al$_5$-GBD magnet, grains with a similar core–shell structure were observed, but the Tb-rich shell was uniformly thinner than that of the Tb$_{100}$-GBD magnet (Fig. 6(d1) and (d3)). In particular, a decrease in the concentrations of Nd and Pr around the Tb-rich shell that was observe for the Tb$_{100}$-GBD magnet was not observed for the Pr$_{60}$Tb$_{20}$Cu$_{15}$Al$_5$-GBD magnet; conversely, an increase in the concentration of Pr at the grain boundary (Fig. 6(d2) and (d4)). This elemental distribution indicated that the large amount of Pr supplied from the diffusion source (Pr$_{60}$Tb$_{20}$Cu$_{15}$Al$_5$) suppressed the excessive substitution of Nd and Pr atoms on the grain surface by Tb atoms from the diffusion source. This enhanced the diffusion efficiency, as shown in Fig. 3(b) and (e).

Next, we performed additional microstructural analyses on the Pr$_{40}$Tb$_{20}$La$_{20}$Cu$_{15}$Al$_5$-, Pr$_{40}$Tb$_{20}$Nd$_{20}$Cu$_{15}$Al$_5$-, and Pr$_{40}$Tb$_{20}$Ce$_{20}$Cu$_{15}$Al$_5$-GBD magnets to investigate the diffusion effect of LREs (La, Nd, and Ce) used to replace Pr. Fig. 7(a) shows the low-magnification elemental mapping images of Tb from the magnet surface to a depth of 450 μm in the GBD magnets. The Tb concentrations in this area increased in the order of Pr$_{40}$Tb$_{20}$La$_{20}$Cu$_{15}$Al$_5$-, Pr$_{40}$Tb$_{20}$Ce$_{20}$Cu$_{15}$Al$_5$-, and Pr$_{40}$Tb$_{20}$Nd$_{20}$Cu$_{15}$Al$_5$-GBD. Fig. 7(b–d) shows the high-magnification backscattered electron (BSE)-SEM and elemental mapping images of the GBD magnets at 100 μm from the magnet surface. The microstructure of the Pr$_{40}$Tb$_{20}$La$_{20}$Cu$_{15}$Al$_5$-GBD magnet exhibited the formation of a uniform and continuous Tb-rich shell (Fig. 7(b1) and (b2)). Pr was distributed in the shell, similar to its distribution in the Pr$_{60}$Tb$_{20}$Cu$_{15}$Al$_5$-
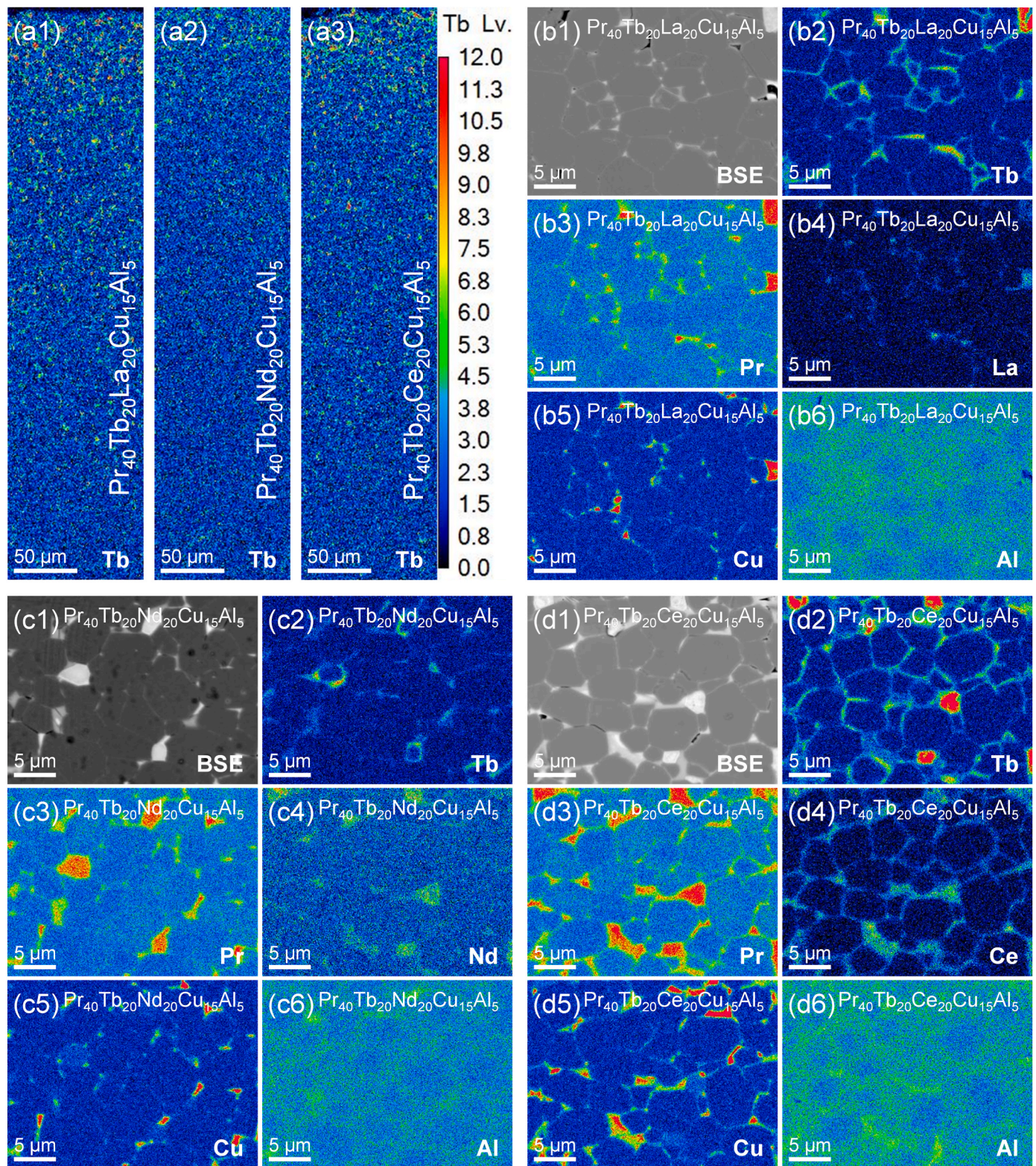
Fig. 7. Low-magnification elemental mapping images of the (a1) $Pr_{40}Tb_{20}La_{20}Cu_{15}Al_5$-, (a2) $Pr_{40}Tb_{20}Nd_{20}Cu_{15}Al_5$, and (a3) $Pr_{40}Tb_{20}Ce_{20}Cu_{15}Al_5$-GBD magnets from the surface to a depth of 450 μm. High-magnification BSE-SEM and elemental mapping images of the (b) $Pr_{40}Tb_{20}La_{20}Cu_{15}Al_5$-, (c) $Pr_{40}Tb_{20}Nd_{20}Cu_{15}Al_5$, and (d) $Pr_{40}Tb_{20}Ce_{20}Cu_{15}Al_5$-GBD magnets at 100 μm from the magnet surface. In each set of six panels, (x1) shows the BSE-SEM image, (x2) the Tb mapping, (x3) the Pr mapping, (x4) the LREs (La, Nd, and Ce) mapping, (x5) the Cu mapping, and (x6) the Al mapping.

GBD magnet, and La was present at similar locations (Fig. 7(b3) and (b4)). This can be attributed to the fact that the E_f of $La_2Fe_{14}B$ is higher than those of $Tb_2Fe_{14}B$ and $Nd_2Fe_{14}B$. Moreover, because the E_f of $La_2Fe_{14}B$ is also higher than that of $Pr_2Fe_{14}B$, it does not suppress the

effect of Pr on the GBD process described above [25]. Therefore, the addition of La reduces the high-cost Pr content of the diffusion source while simultaneously maintaining the effect of suppressing the excessive lattice diffusion of Tb.
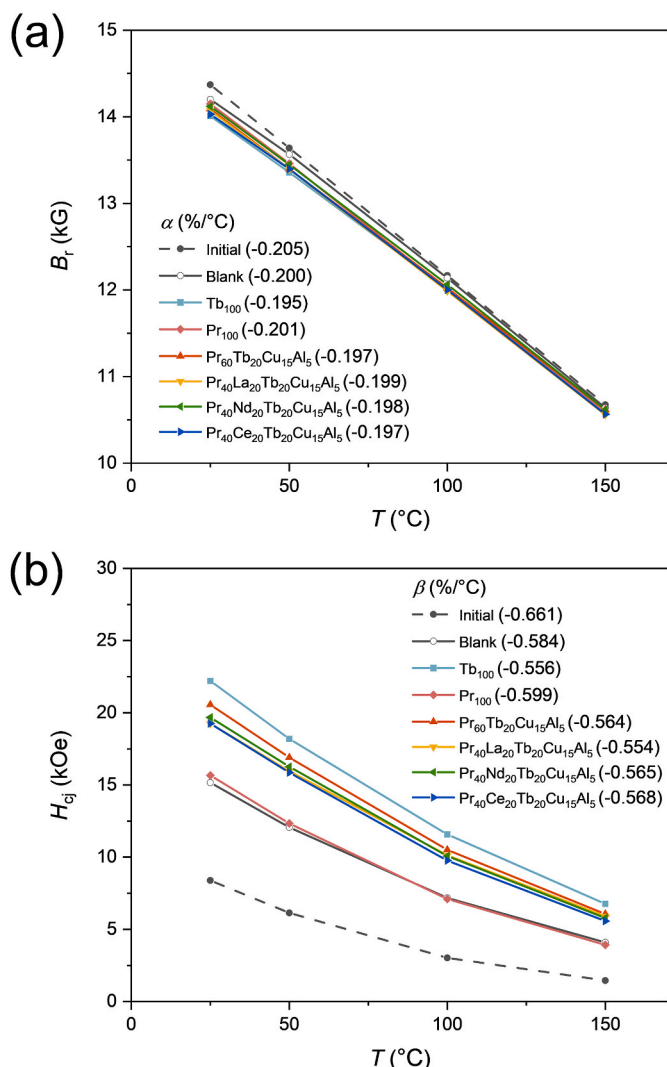
Fig. 8. The temperature dependence of (a) B_r and (b) H_{cj} of the initial, blank, and Tb$_{100}$-, Pr$_{100}$-, Tb$_{60}$Pr$_{20}$Cu$_{15}$Al$_5$-, Tb$_{40}$Pr$_{20}$La$_{20}$Cu$_{15}$Al$_5$-, Tb$_{40}$Pr$_{20}$Nd$_{20}$Cu$_{15}$Al$_5$-, and Tb$_{40}$Pr$_{20}$Ce$_{20}$Cu$_{15}$Al$_5$-GBD magnets within the temperature range of 25–150 °C.

In the Pr$_{40}$Tb$_{20}$Nd$_{20}$Cu$_{15}$Al$_5$-GBD magnet, a relatively nonuniform and discontinuous Tb-rich shell was observed compared to that in the Pr$_{40}$Tb$_{20}$La$_{20}$Cu$_{15}$Al$_5$-GBD magnet (Fig. 7(c1) and (c2)). Moreover, the aggregation of Pr at the triple junction increased, and unlike La, Nd was present at different locations from that of Pr (Fig. 7(c3) and (c4)). This is because the E_f of Nd$_2$Fe$_{14}$B is lower than that of Pr$_2$Fe$_{14}$B, suggesting that it suppresses not only the lattice diffusion of Pr but also the formation of a Tb-rich shell [25]. The microstructure of the Pr$_{40}$Tb$_{20}$Ce$_{20}$-Cu$_{15}$Al$_5$-GBD magnet shows the most distinct Tb-rich shell formation among these three GBD magnets (Fig. 7(d1) and (d2)). However, Pr accumulation was observed most frequently and a distinct Ce-rich shell was formed (Fig. 7(d3) and (d4)). This microstructure can be attributed to the lower E_f of Ce$_2$Fe$_{14}$B compared to that of the Nd$_2$Fe$_{14}$B main phase [25]. Moreover, the formation of a Ce-rich shell results in a decrease in the B_r and $(BH)_{max}$ of the GBD magnet, as was observed in Fig. 3(a) and (c), because the Ce$_2$Fe$_{14}$B phase has the lowest saturation magnetization value among the LRE$_2$Fe$_{14}$B phases [25,36].

Fig. 7(b5–d5) and (b6–d6) show the Cu and Al mapping images of the GBD magnets, respectively. Cu was mainly found in the triple junction and in small amounts at the grain boundaries, whereas Al was widely distributed around the grain boundaries. These low-melting point metals were employed to improve the wettability of the grain boundary phase,

thus promoting the formation of uniform and continuous Tb-rich shells and grain boundaries between the Nd$_2$Fe$_{14}$B matrix phases [29,37]. In particular, the Pr$_{40}$Tb$_{20}$Ce$_{20}$Cu$_{15}$Al$_5$-GBD magnets exhibited pronounced grain boundary distribution of Cu and lattice diffusion of Al, which is attributed to the low melting point of Ce and the low formation energy of the Ce$_2$Fe$_{14}$B phase.

Finally, the thermal stabilities of the initial, blank, and Tb$_{100}$-, Pr$_{100}$-, Pr$_{60}$Tb$_{20}$Cu$_{15}$Al$_5$-, Pr$_{40}$Tb$_{20}$La$_{20}$Cu$_{15}$Al$_5$-, Pr$_{40}$Tb$_{20}$Nd$_{20}$Cu$_{15}$Al$_5$-, and Pr$_{40}$Tb$_{20}$Ce$_{20}$Cu$_{15}$Al$_5$-GBD magnets were investigated. Fig. 8 shows the temperature dependence of B_r and H_{cj} in the temperature range of 25–150 °C for the magnets. The B_r and H_{cj} of the Nd–Fe–B sintered magnets gradually decreased with temperature owing to the thermal disturbance effect [38]. The thermal stability of the magnets was quantitatively evaluated by the temperature coefficients α = [Br (T2) − Br (T1)]/[Br (T1) × (T2 − T1)] and β = [Hcj (T2) − Hcj (T1)]/[Hcj (T1) × (T2 − T1)] defined based on the temperature dependence of Br and Hcj [39]. A decrease in the absolute value of the temperature coefficients indicates an improvement in thermal stability. Although the changes of B$_r$ were not considerable, |α| decreased slightly for the blank and GBD magnets (Fig. 8(a)). Conversely, significant decreases in |β| were obtained for the blank and GBD magnets, indicating an improvement in the thermal stability of H$_{cj}$ through the heat-treatment and GBD processes (Fig. 8(b)). The Pr$_{40}$Tb$_{20}$La$_{20}$Cu$_{15}$Al$_5$-GBD magnet exhibited the largest decrease in |β| (−0.554 %/°C) compared to that of the initial magnet (−0.661 %/°C), which was even lower than that of the Tb$_{100}$-GBD magnet (−0.556 %/°C). This is consistent with previous GBD magnet study that reported enhanced thermal stability with La-containing sources [40].

4. Conclusions

We demonstrated a stamp coating method based on powder-type diffusion sources that excludes solution exposure and realized a reduction in the use of high-cost HREs and LREs in the GBD process to improve the magnetic performance of Nd–Fe–B sintered magnets. First, the feasibility of stamp coating was verified through a systematic comparison of various dip-coated samples based on 1 wt% Tb. Second, to reduce HRE usage, the GBD of diffusion sources with 80 wt% Tb replaced with Pr and transition metals was tested via the stamp coating. Third, to reduce the usage of high-cost LREs, the GBD of diffusion sources with 20 wt% of Pr replaced by La, Nd, or Ce was investigated. In conclusion, we validated the effectiveness of a simplified stamp coating method and identified diffusion sources that achieved magnetic properties equivalent to those of pure Tb-GBD magnets while reducing Tb usage by 80 wt %. Furthermore, by elucidating and utilizing the mechanism, we identified La as a replacement element that can reduce the use of high-cost Pr, which was used to replace Tb. These results provide valuable guidance for optimizing the microstructure of GBD magnets based on the formation energy and magnetic properties of the RE–Fe–B matrix, thereby increasing the efficiency of GBD in improving magnetic properties while reducing process costs.

Declaration of competing interest

The authors declared that they have no conflicts of interest to this work. We declare that we do not have any commercial or associative interest that represents a conflict of interest in connection with the work submitted.

Acknowledgments

References

[1] Gutfleisch O, Willard MA, Brück E, Chen CH, Sankar S, Liu JP. Magnetic materials and devices for the 21st century: stronger, lighter, and more energy efficient. Adv Mater 2011;23(7):821–42.

[2] Sagawa M, Fujimura S, Togawa N, Yamamoto H, Matsuura Y. New material for permanent magnets on a base of Nd and Fe. J Appl Phys 1984;55(6):2083–7.

[3] Hono K, Sepehri-Amin H. Prospect for HRE-free high coercivity Nd-Fe-B permanent magnets. Scr Mater 2018;151:6–13.

[4] Sugimoto S. Current status and recent topics of rare-earth permanent magnets. J Phys Appl Phys 2011;44(6):064001.

[5] Hioki K. High performance hot-deformed Nd-Fe-B magnets. Sci Technol Adv Mater 2021;22(1):72–84.

[6] Hono K, Sepehri-Amin H. Strategy for high-coercivity Nd–Fe–B magnets. Scr Mater 2012;67(6):530–5.

[7] Nakamura H, Hirota K, Shimao M, Minowa T, Honshima M. Magnetic properties of extremely small Nd-Fe-B sintered magnets. IEEE Trans Magn 2005;41(10):3844–6.

[8] Coey J. Permanent magnets: plugging the gap. Scr Mater 2012;67(6):524–9.

[9] Hirosawa S, Matsuura Y, Yamamoto H, Fujimura S, Sagawa M, Yamauchi H. Magnetization and magnetic anisotropy of R2Fe14B measured on single crystals. J Appl Phys 1986;59(3):873–9.

[10] Chen B, et al. Design and fabrication of Dy-free sintered permanent magnets with high coercivity. J Appl Phys 2012;111(7).

[11] Sepehri-Amin H, Ohkubo T, Hono K. The mechanism of coercivity enhancement by the grain boundary diffusion process of Nd–Fe–B sintered magnets. Acta Mater 2013;61(6):1982–90.

[12] He J, et al. Grain boundary diffusion sources and their coating methods for Nd-Fe-B permanent magnets. Metals 2021;11(9):1434.

[13] Zhou T, Liu R, Qu P, Xie G, Li M, Zhong Z. Diffusion behavior and coercivity enhancement of Tb-containing NdFeB magnet by dip-coating TbH3. J Mater Res Technol 2022;20:1391–8.

[14] Jang YR, et al. Microstructure of shell and grain boundary phase in Nd-Fe-B sintered magnets grain boundary diffusion processed with low-melting LRE-Al-Cu (LRE= La and Pr) alloys. Mater Char 2024;216:114249.

[15] Li W, et al. Formation of anti-shell/core structure of heavy rare earth elements (Tb, Dy) in sintered Nd-Fe-B magnet after grain boundary diffusion process. Scr Mater 2019;163:40–3.

[16] Jang YR, et al. Dependence of magnetic performance on coating method in grain boundary diffusion processed Nd-Fe-B sintered magnets. Mater Today Commun 2024;38:108004.

[17] Cao X, et al. Coercivity enhancement of sintered Nd–Fe–B magnets by efficiently diffusing DyF3 based on electrophoretic deposition. J Alloys Compd 2015;631: 315–20.

[18] He J, Song W, Liu X, Yu H, Zhong X, Liu Z. High-efficient selected area grain boundary diffusion for enhancing the coercivity of thick Nd-Fe-B magnets. Appl Phys Lett 2022;120(4).

[19] Ji M, et al. The reinforcement strategy of electrophoretic deposition coating assisted by PVP for grain boundary diffusion of Nd-Fe-B magnet. J Mater Res Technol 2024;28:3068–75.

[20] Woo HJ, Kim JH. Preparation of nanofibrillated cellulose and its effect on the properties of PVA composite film. POLYMER-KOREA 2018;42(1):52–8.

[21] Wong Y, Chang H, Chang W. Coercivity enhancement with reduced Tb usage for NdFeB sintered magnets by grain boundary diffusion with multicomponent Tb-Ce-Al-Cu-Zn alloy powders. J Magn Magn Mater 2024;589:171586.

[22] Zhao L, et al. Understanding the role of element grain boundary diffusion mechanism in nd–fe–b magnets. Adv Funct Mater 2021;32(8).

[23] Lan TTB, Hermosa GC, Sun A-C. Enhanced perpendicular magnetic anisotropy of sputtered Pr-Fe-B thin film by inter-layer diffusion Fe–Si layer. J Phys Chem Solid 2020;144:109506.

[24] Yan M, et al. Merits of Pr80Ga20 grain boundary diffusion process towards high coercivity–remanence synergy of Nd−La−Ce−Fe−B sintered magnet. Acta Mater 2022;231:117873.

[25] He J, Zhou B, Liao X, Liu Z. Nanocrystalline alternative rare earth-iron-boron permanent magnets without Nd, Pr, Tb and Dy: a review. J Mater Res Technol 2024;28:2535–51.

[26] Kim T-H, et al. Anisotropic diffusion mechanism in grain boundary diffusion processed Nd–Fe–B sintered magnet. Acta Mater 2016;112:59–66.

[27] Kim T-H, Lee S-R, Kim H-J, Lee M-W, Jang T-S. Simultaneous application of Dy–X (X= F or H) powder doping and dip-coating processes to Nd–Fe–B sintered magnets. Acta Mater 2015;93:95–104.

[28] Zhang Y, et al. Squareness factors of demagnetization curves for multi-main-phase Nd-Ce-Fe-B magnets with different Ce contents. J Magn Magn Mater 2019;487: 165355.

[29] Lee DH, et al. Coercivity and thermal stability enhancement of Nd-Fe-B sintered magnets by grain boundary diffusion with Tb-Al-Cu alloys. Materialia 2024;36: 102161.

[30] Pope CG. X-ray diffraction and the bragg equation. J Chem Educ 1997;74(1):129.

[31] Zhou T, et al. Coercivity and thermal stability enhancement of NdFeB magnet by grain boundary diffusion Tb80Al20 alloys. Intermetallics 2021;138:107335.

[32] Shannon RD. Revised effective ionic radii and systematic studies of interatomic distances in halides and chalcogenides. Foundations of Crystallography 1976;32 (5):751–67.

[33] Song X, et al. Strategies for efficient utilization of heavy rare-earth Tb in high-performance Ce magnets with high Ce content. J Mater Res Technol 2024;33: 8655–65.

[34] Yang E, et al. Evolution of Tb-shell homogeneity in Nd-Fe-B sintered magnets by long-term Tb grain boundary diffusion. J Alloys Compd 2023;963:171236.

[35] Samardžija Z, McGuiness P, Soderžnik M, Kobe S, Sagawa M. Microstructural and compositional characterization of terbium-doped Nd–Fe–B sintered magnets. Mater Char 2012;67:27–33.

[36] Herbst J. R 2 Fe 14 B materials: intrinsic properties and technological aspects. Rev Mod Phys 1991;63(4):819.

[37] Zhang X, et al. Modifying Tb-Cu grain boundary diffusion behavior in Nd-Fe-B magnets by Gd or other rare earth elements. Mater Chem Phys 2024;314.

[38] Zhou TJ, et al. Effect of diffusing TbH3 on magnetic, corrosion and mechanical properties of NdFeB magnet. J Alloys Compd 2023;968 (in English).

[39] Brown D, Ma B-M, Chen Z. Developments in the processing and properties of NdFeB-type permanent magnets. J Magn Magn Mater 2002;248:432–40.

[40] Zeng HX, et al. Grain boundary diffusion treatment of sintered NdFeB magnets by low cost La-Al-Cu alloys with various Al/Cu ratios. J Magn Magn Mater 2019;490: 165498.